Published on 30 July 2018. Downloaded by Ulsan National Institute of Science & Technology (UNIST) on 8/20/2018 1:57:25 AM.

Nanoscale

PAPER

View Article Online
View Journal

Check for updates

Cite this: DOI: 10.1039/c8nr02883d

Diffusion controlled multilayer electrocatalysts *via* graphene oxide nanosheets of varying sizes†

Minsu Gu,*[a] Jaewon Choi,[a] Taemin Lee,[a] Minju Park,[a] Ik-Soo Shin,[b] Jinkee Hong,[c] Hyun-Wook Lee[a] and Byeong-Su Kim*[a,d]

Received 10th April 2018,
Accepted 27th July 2018

DOI: 10.1039/c8nr02883d

rsc.li/nanoscale

Controlling the architecture of hybrid nanomaterial electrodes is critical for understanding their fundamental electrochemical mechanisms and applying these materials in future energy conversion and storage systems. Herein, we report highly tunable electrocatalytic multilayer electrodes, composed of palladium nanoparticles (Pd NPs) supported by graphene sheets of varying lateral sizes, employing a versatile layer-by-layer (LbL) assembly method. We demonstrate that the electrocatalytic activity is highly tunable through the control of the diffusion and electron pathways within the 3-dimensional multilayer electrodes. A larger-sized-graphene-supported electrode exhibited its maximum performance with a thinner film, due to facile charge transfer by the mass transfer limited in the early stage, while a smaller-sized-graphene-supported electrode exhibited its highest current density with higher mass loading in the thicker films by enabling facile mass transfer through increased diffusion pathways. These findings of the tortuous-path effect on the electrocatalytic electrode supported by varying sized graphene provide new insights and a novel design principle into electrode engineering that will be beneficial for the development of effective electrocatalysts.

Introduction

The rapidly approaching energy crisis necessitates efficient conversion and storage technologies for sustainable and renewable energy to diminish the current environmental concerns that are growing unabated.[1] In this regard, energy devices with superior performance have been developed such as fuel cells, metal–air batteries, and water electrolyzers, all of which use highly efficient and cost-effective electrocatalysts during electrochemical operation.[2–5] Thus, there has been significant progress in the development of various electrocatalysts such as novel metal nanoparticles (NPs) and carbon-based nanomaterials.[5,6] These active materials are generally applied in the form of composites combined with conductive supports and binders to compensate for their drawbacks such as volume expansion, low electrical conductivity, and poor cycling performance. Catalytic supports are critical in the performance of electrocatalysts and, consequently, there are continuing efforts to develop effective conductive supports.[7,8]

Graphene oxide (GO), a chemically exfoliated graphene analogue, serves as a unique electrocatalytic support with its large surface area, chemical functionality, and remarkable mechanical/chemical stability.[9–11] Owing to the atomically thin 2-dimensional (2D) sheet structure of GO, significant efforts have been devoted to enhancing the catalytic performance of various electroactive nanomaterials, such as metals, metal oxides, and semiconductors, on the surface of 2D materials as well as GO.[12–17] Furthermore, the importance of controlling the GO sheet size has recently been illustrated by their size-dependent electrochemical activity; for example, the Li group demonstrated that the large size of chemically synthesized graphene quantum dots showed the increased electrocatalytic activity toward the oxygen reduction reaction.[18] Conversely, the Chen group reported that using smaller GO sheets improved the heterogeneous electron transfer kinetics in the reduction of redox probes within the electrode, which was correlated with an increased defect density in smaller GO sheets.[19] Consequently, using GO nanosheets with a well-defined lateral size is important when utilizing GO electrode materials in electrochemical reactions. However, the as-synthesized GO products often have a wide size distribution due to the uncontrolled breakage of large sheets into small sheets during the oxidation and exfoliation processes. There are outstanding contributions to controlling the size fractionation of GO

[a]Department of Energy Engineering, Ulsan National Institute of Science and Technology (UNIST), Ulsan 44919, Korea. E-mail: sbgms@unist.ac.kr, bskim19@unist.ac.kr
[b]Department of Chemistry, Soongsil University, Seoul 06978, Korea
[c]Department of Chemical and Biomolecular Engineering, Yonsei University, Seoul 03722, Korea
[d]Department of Chemistry, Ulsan National Institute of Science and Technology (UNIST), Ulsan 44919, Korea

†Electronic supplementary information (ESI) available. See DOI: 10.1039/c8nr02883d

Published on 30 July 2018. Downloaded by Ulsan National Institute of Science & Technology (UNIST) on 8/20/2018 1:57:25 AM.

nanosheets that exploit differences in the molecular weight and charge density between GO nanosheets of varied sizes using methods such as centrifugation, pH-assisted sedimentation, and dispersibility in polar solvents.[19–22]

Utilizing electrode fabrication techniques that allow nanoscale blending of materials is also important when investigating the nanoscopic electrochemical activity of graphene-supported hybrid nanomaterials. This contrasts with bulk graphene composites that are traditionally prepared by a simple mixing process. Layer-by-layer (LbL) assembly is one of the most versatile tools used to assemble multifunctional nanoscale materials with nanoscale control over their composition and structure.[23–26] Generally, the LbL-assembled films are formed by depositing alternating layers of oppositely charged materials. Due to its simplicity and versatility as a method, the LbL-assembled thin films have been examined for various energy conversion and storage devices.[11,27–32] For example, the Shao-Horn and Lutkenhaus groups independently showed the tunable electrocatalytic activity of LbL-assembled electrodes, emphasizing the excellent charge-storage capability of carbon nanotubes and GO nanosheets.[33,34] Interestingly, these studies indicate that the electrochemical activity can be tuned by varying the number of bilayers (*i.e.* thickness). This phenomenon is attributed to the balance between electron transfer into the inner electrode surface and ionic transport from the electrolyte that are restricted with increasing multilayer film thickness.[32,35] In another notable example, our group found that the performance of graphene-supported metal NP-based electrocatalysts exhibited the maximum performance at a specific thickness and optimized layer sequence within the multilayer electrodes.[36,37] Although there are some examples to enhance mass transfer by structurally deformed 2D materials,[38,39] including our own efforts, demonstrating the electrocatalytic performance of the 3D multilayer electrodes, there are few studies achieving such fine control over the electrocatalytic behavior simply by changing the dimension of the individual components which unravels the underlying electrochemical mechanism between mass and charge transfer thus far.

Herein, we report the fabrication of elaborately designed electrodes using an LbL assembly method that enables control over the internal electrode structure and mass-transfer pathways by varying the size of the GO building blocks. Specifically, to investigate the influence of controlled diffusion pathways within the 3D LbL-assembled electrodes on their electrocatalytic activity, we prepared three GO suspensions with different GO sheet size distributions and assembled them with Pd NPs to fabricate hybrid electrocatalytic electrodes. We then used the methanol oxidation reaction (MOR) as a model reaction to investigate their activity (Scheme 1). The electrocatalytic activity toward the MOR is highly affected by the balance between the mass-transfer pathway and charge transfer within the electrode, which varies with the GO sheet dimensions. This interesting model system offers a unique opportunity to understand the fundamental electrochemical mechanisms of hybrid multilayer electrodes composed of identical components, which is vital for designing high-performance electrocatalysts.

Experimental

Materials

Graphite powder, 4-(dimethylamino)pyridine, sodium tetrachloropalladate(II) (Na_2PdCl_4) and (3-aminopropyl)triethoxysilane were purchased from Sigma-Aldrich. Graphite nanofibers were purchased from Catalytic Materials (United States).

Preparation of LGO

Graphite oxide was synthesized from graphite powder by the modified Hummers method and exfoliated to give a brown dispersion of LGO using a homogenizer (WiseTis, HG-15D) at a concentration of 0.50 mg mL^{-1}.[40,41]

Preparation of MGO

Graphite oxide was exfoliated under ultrasonication (Sonics & Materials Inc., VC 750) at a concentration of 0.50 mg mL^{-1}.[42]

Preparation of NGO

NGO was synthesized from graphite nanofibers according to a literature method under ultrasonication at a concentration of 0.50 mg mL^{-1}.[43]

Preparation of Pd NPs

The 4-(dimethylamino)pyridine (DMAP)-stabilized Pd NPs were prepared by using the spontaneous phase transfer from an organic solvent according to a literature method.[44]

Layer-by-layer assembly of hybrid electrode films

An ITO-coated glass substrate was cleaned by sonication in deionized (DI) water, acetone and ethanol for 10 min. Silicon and quartz substrates were cleaned by piranha solution to remove any organic contamination and subsequently treated with (3-aminopropyl)triethoxysilane to introduce a positively charged hydrophilic surface. These substrates were first dipped into a negatively charged GO solution (0.50 mg mL^{-1}) at pH 4 for 10 min. They were then dipped into DI water for 1 min three times to remove loosely bound GO. Subsequently, the substrates were then dipped into positively charged DMAP-coated Pd NP suspension at pH 11 for 10 min, and washed with DI water three times for 1 min, which afforded one-bilayer film of $(GO/Pd)_1$. The above procedures were repeated to achieve the desired number of bilayers (BL, n).

Electrochemical analysis

The as-assembled multilayer films were subjected to a thermal reduction process at 150 °C for 12 h in an oven before investigating the electrochemical properties. Electrochemical experiments were performed using a standard three electrode cell configuration (Biologic Science Instruments, VSP). A platinum wire was used as a counter electrode and Hg/HgO as a reference. The working electrode was a multilayer thin film

 This journal is © The Royal Society of Chemistry 2018

Published on 30 July 2018. Downloaded by Ulsan National Institute of Science & Technology (UNIST) on 8/20/2018 1:57:25 AM.

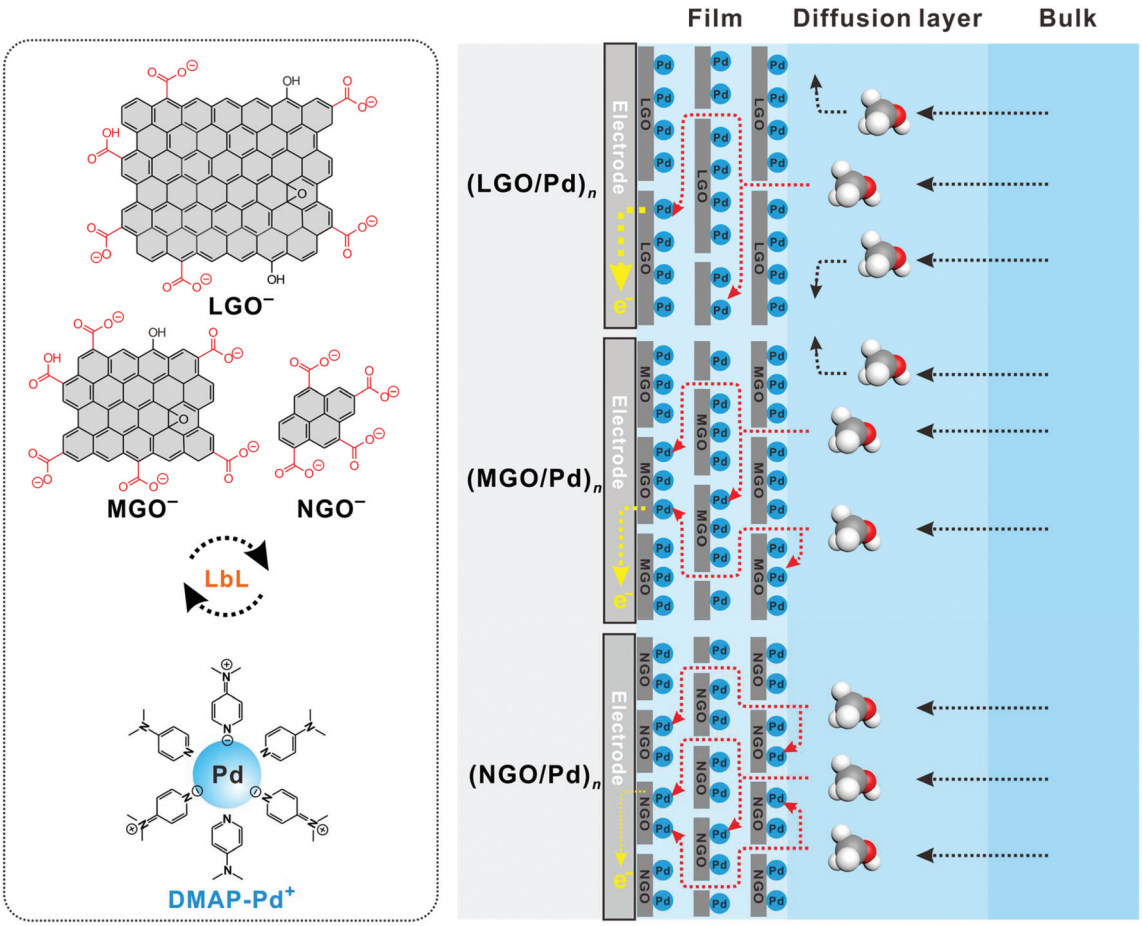

Scheme 1 Schematic representation of layer-by-layer (LbL)-assembled $(GO/Pd)_n$ multilayer thin film electrodes with varying GO sheet sizes (LGO, MGO, and NGO) toward methanol oxidation reaction in bulk electrolyte solution. The black and red dotted arrows indicate the diffusion of methanol molecules into electrolyte and the 3D LbL electrodes, respectively. The yellow arrows indicate the charge transfer from the 3D LbL electrodes.

assembled on ITO-coated glass. Cyclic voltammetry (CV) was performed between −0.60 and 0.60 V in 0.10 M KOH solution with 1.0 M methanol solution at room temperature in saturated N_2 at a scan rate of 20 mV s^{-1}. Electrochemical impedance spectroscopy (EIS) measurements were carried out in the frequency range from 100 kHz to 50 mHz under an AC stimulus of 10 mV in amplitude.

Characterization

FT-IR (Varian, 670-IR) and Raman spectroscopy (WITec, alpha300R) were used to determine the chemical structure of varying GO sheets. The size and morphology of the prepared NPs were measured by transmission electron microscopy (Normal-TEM, JEOL, JEM-2100, accelerating voltage of 200 kV). The absorbance of the thin films was characterized by using UV/vis spectroscopy (Varian, Cary 5000). The thickness of the as-prepared samples on silicon substrates was measured by using a surface profiler (Veeco, Dektak 150). The surface morphology of the samples was investigated using scanning electron microscopy (Cold FE-SEM, Hitachi, S-4800) and atomic force microscopy (AFM, Veeco, Dimension D3100) *via* a tapping mode. The active mass of each material adsorbed onto the film surface was analyzed by using a quartz crystal microbalance (QCM, Stanford Research Systems, QCM200), using the following Sauerbrey eqn (1) and (2):

$$\Delta F(\mathrm{Hz}) = -\frac{2{F_o}^2}{A\sqrt{\rho_q \mu_q}}\Delta m \quad (1)$$

$$\Delta F(\mathrm{Hz}) = -56.6 \times \Delta m \quad (2)$$

where ΔF is the resonant frequency change (Hz), Δm is the mass change per unit area of the quartz crystal (μg cm^{-2}), F_o (5 MHz) is the fundamental resonance frequency of the crystal, A is the area of the Au–Cr electrode, ρ_q (2.65 g cm^{-3}) is the density of the quartz crystal and μ_q (2.95×10^{11} g cm^{-1} s^{-2}) is the shear modulus.

Results and discussion

Highly stable aqueous GO suspensions and electrocatalytic Pd NPs are prerequisites for fabricating 3D LbL multilayer electrodes based on electrostatic interactions. In order to prepare GO

Published on 30 July 2018. Downloaded by Ulsan National Institute of Science & Technology (UNIST) on 8/20/2018 1:57:25 AM.

suspensions of varying size, graphite powder was initially oxidized according to the modified Hummers method to obtain graphite oxide, which contains various chemical functional groups such as carboxyl acid, hydroxyl, and epoxide groups.[40,41] We then utilized two different exfoliation methods using homogenization and ultrasonication to prepare GO suspensions with different size distributions. Homogenization was used as a mild exfoliation method to produce a lower-defect GO by shear stress, resulting in a suspension of large-sized graphene (LGO) sheets, while medium-sized GO (MGO) sheets were prepared using ultrasonication, which tears the graphene sheets and introduces more damage.[42] In addition, we prepared nanosized graphene (NGO) sheets according to a literature method using exfoliation from a graphite nanofiber precursor, which has smaller carbon domains than conventional graphite powder.[43]

The successful synthesis of the three GO sheet suspensions was confirmed by atomic force microscopy (AFM) and Fourier-transform infrared (FT-IR) spectroscopy measurements. Representative AFM images revealed that all the GO suspensions were mainly composed of single-layer GO sheets, with a thickness of ~1.4 nm (Fig. 1). Each GO suspension exhibited a distinct lateral-size distribution, with average dimensions of 52.61 ± 50.88, 0.57 ± 0.22, and $0.38 \times 10^{-3} \pm 0.17 \times 10^{-3}$ μm^2 for LGO, MGO, and NGO, respectively. This indicates that using different exfoliation processes and precursors was successful in controlling the GO sheet size.

FT-IR spectroscopy was employed to characterize the chemical functionalities present in LGO, MGO, and NGO (see Fig. S1 in the ESI†). All three GO products showed the carbonyl-stretching vibration peaks associated with carboxylic acid (COOH, at 1722 cm^{-1}) and carboxylate groups (COO^-, at 1600 cm^{-1}). The relative fraction of the carboxylate to carboxylic acid at pH 4 was determined to be 0.75, 1.20, and 3.86 for LGO, MGO, and NGO, respectively. This indicates that the ionization of the GO sheets is significantly affected by the density of chemical functional groups on the GO sheets due to the structural difference induced by the number of defects within the GO sheets.

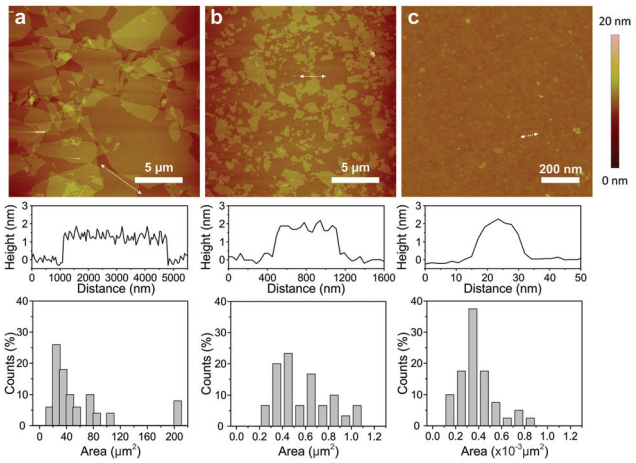

Fig. 1 Representative AFM images of (a) LGO, (b) MGO, and (c) NGO sheets with the corresponding line scan profiles and size distribution histograms. The average values were collected over 40 samples.

Raman spectroscopy analysis was used to further investigate the structural differences between the three GO products (see Fig. S2 in the ESI†). Generally, GO displays two prominent peaks at 1344 and 1601 cm^{-1}, which corresponded to the symmetry A_{1g} mode of the D band and the E_{2g} mode of the sp^2 carbon atoms of the G band, respectively.[45] It is well established that the D band corresponds to structural defects, amorphous structures, or edges that break the sp^2-carbon-lattice symmetry, while the G band is associated with graphitic sp^2-carbon domains. A strong D-band intensity indicates a high defect density and the presence of edge functional groups in GO. The D-to-G-band intensity ratio (I_D/I_G) was 0.99, 1.04, and 1.09 for LGO, MGO, and NGO, respectively, suggesting that the sp^2 carbon structure becomes more damaged with decreasing GO sheet dimensions.

In parallel, a positively charged Pd NP suspension was prepared based on the spontaneous phase transfer of organic-soluble Pd NPs into an aqueous phase using 4-(dimethylamino)pyridine (DMAP), a readily available organic ligand that affords the necessary stability in aqueous solutions.[44] The resulting DMAP-coated Pd NPs had an average diameter of 3.4 ± 0.5 nm (see Fig. S3 in the ESI†).

With these stable suspensions of the positively charged Pd NPs (ζ-potential of +35 mV) as electroactive species and the negatively charged GO suspension (ζ-potential of −40 mV) as a stable catalytic support, we fabricated three types of multilayer electrodes by LbL assembly using LGO, MGO, and NGO. The resulting multilayer architectures were denoted as $(LGO/Pd)_n$, $(MGO/Pd)_n$, and $(NGO/Pd)_n$, where n is the number of GO/Pd bilayers (BLs, typically 2–10). UV/vis spectroscopy was used to monitor the successful growth of each multilayer (Fig. 2a and Fig. S4 in the ESI†). The absorbance gradually increased with increasing number of layers, indicating the successful assembly of GO-supported-Pd NP multilayer electrodes. Moreover, the linear growth of the characteristic GO absorbance peak at 215 nm clearly demonstrated the uniform formation of multilayers with respect to the number of BLs. The corresponding thickness of each multilayer film grew linearly with the number of BLs and the average bilayer thickness was 8.5, 8.5, and 10.1 nm for a single bilayer of $(LGO/Pd)_n$, $(MGO/Pd)_n$, and $(NGO/Pd)_n$, respectively (Fig. 2b). These similar film thicknesses are attributed to the well-exfoliated nature of the single-layer GO regardless of the sheet size. It should be noted that the internal architecture of the hybrid electrodes could be controlled precisely by the LbL assembly method with high accuracy.

We further analyzed the sequential adsorption behavior of GO and Pd NPs in each multilayer electrode using a quartz crystal microbalance (QCM). Fig. 2c shows the stepwise measurement of the mass deposited after each layer, which quantifies the amount of each component in the multilayer structure. The adsorption of Pd NPs was greater than that of the GO sheets, with the relative mass ratio of GO to Pd NPs

 This journal is © The Royal Society of Chemistry 2018

Published on 30 July 2018. Downloaded by Ulsan National Institute of Science & Technology (UNIST) on 8/20/2018 1:57:25 AM.

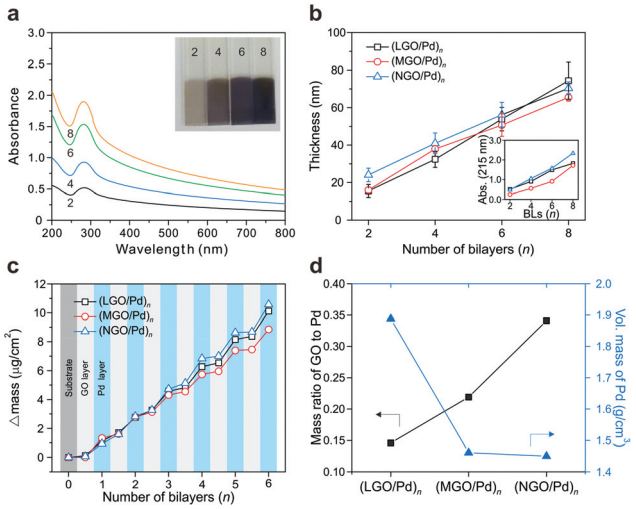

Fig. 2 (a) UV/vis absorbance spectra of representative $(LGO/Pd)_n$ multilayer thin films. The inset image shows the samples prepared with the corresponding number of bilayers (BLs, *n*). (b) Film thickness measured by surface profiler and (c) quartz crystal microbalance (QCM) analysis of all multilayer thin film electrodes as a function of the number of BLs (*n*). The inset in b shows the corresponding UV/vis absorbance maxima at 215 nm for all multilayer electrodes. (d) Mass ratio of GO to Pd and volumetric mass of Pd in each multilayer thin film.

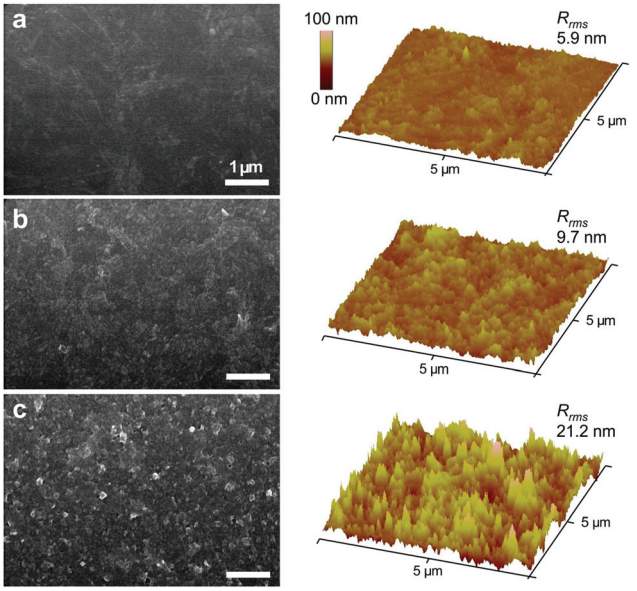

Fig. 3 Representative SEM (left) and AFM (right) images of (a) $(LGO/Pd)_4$, (b) $(MGO/Pd)_4$, and (c) $(NGO/Pd)_4$ multilayer thin film electrodes. The scale bar in the SEM images is 1 μm and the R_{rms} values of the AFM images are averaged over a 5 × 5 μm^2 area.

within each multilayer found to be 0.146, 0.219, and 0.341 on the surface of LGO, MGO, and NGO, respectively (Fig. 2d). This could be attributed to decreasing GO sheet density per single-layer unit area with decreasing GO sheet size. In addition, we calculated the volumetric mass of Pd NPs within each multilayer based on the film thickness determined. The volumetric mass of Pd NPs within each layer decreased from 1.89 to 1.45 as the GO sheet size decreased from LGO to NGO, indicating a change in the 3D multilayer electrode morphology from relatively densely packed films to porous films.

Analyzing the surface morphology of each film also supports the assembled multilayer films (Fig. 3). Scanning electron microscopy (SEM) measurements with the corresponding elemental mapping images showed that the substrate surfaces were successfully covered with uniformly deposited Pd NPs on top of GO sheets in all multilayers of $(LGO/Pd)_n$, $(MGO/Pd)_n$, and $(NGO/Pd)_n$ (Fig. S5 in the ESI†). The surface morphology of the assembled films exhibited characteristic wrinkled GO sheets of varying sizes, distributed over the entire film surface. In addition, the films assembled with NGO nanosheets displayed a relatively rough morphology, with root-mean-square roughness (R_{rms}) values of 5.9, 9.7, and 21.2 nm determined from the AFM measurements for the $(LGO/Pd)_4$, $(MGO/Pd)_4$, and $(NGO/Pd)_4$ films, respectively.

The change in surface roughness by graphene sheet size was further confirmed by cross-sectional high-resolution transmission electron microscopy (HR-TEM), clearly indicating the different surface morphologies with respect to the dimension of GO sheets within the multilayers (Fig. 4). In addition, the identification of the precise nanoscale architecture was elucidated by cross-sectional high-angle annular dark field scanning transmission electron microscopy (HAADF-STEM) with corresponding electron energy loss spectroscopy (EELS). The HAADF-STEM image demonstrated the homogeneous lateral distribution of respective components with the corresponding EELS line scan analysis of $(LGO/Pd)_6$ multilayer films clearly distinguishing the alternate deposition of LGO sheets and Pd NP layers through a sequential nanoscale control enabled by LbL assembly.

An increased electrode surface roughness can enhance the interactions between the Pd NPs within the multilayer and the electrolyte, leading to increased diffusion pathways for the reactants into the inner multilayer electrode. This tortuous-path effect created by the layered architecture of the 2D materials in the multilayer films has been similarly demonstrated in barrier films that block the diffusion of permeable gases or liquids.[46,47] However, the effect on electrocatalytic films by the tortuous-path has not been studied intensively with quantitative electrochemical comparison such as the mass-transfer process of electroactive species from the diffusion layer of the electrolyte into the surface of the electrode.

In order to electrochemically investigate the influence of increased diffusion pathways with varying GO sizes, cyclic voltammetry was performed to evaluate the electrochemical performance of the multilayer electrodes toward the MOR (Fig. 5). The MOR is a particularly interesting model reaction, as it allows the assessment of the mass transfer (diffusion of methanol molecules from the electrolyte) and charge transfer (dissociation of methanol molecules by C–H bond breaking)

Published on 30 July 2018. Downloaded by Ulsan National Institute of Science & Technology (UNIST) on 8/20/2018 1:57:25 AM.

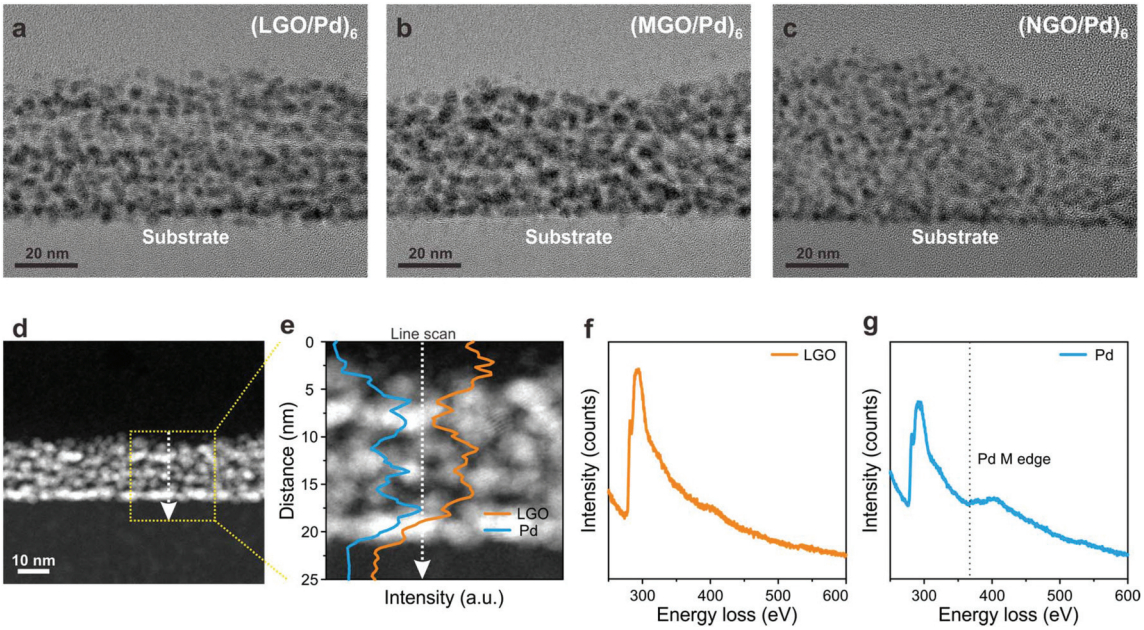

Fig. 4 (a–c) Representative cross-sectional high-resolution TEM images of (a) $(LGO/Pd)_6$, (b) $(MGO/Pd)_6$, and (c) $(NGO/Pd)_6$ multilayer thin film electrodes. (d) Representative cross-sectional HAADF-STEM image of $(LGO/Pd)_6$ with (e) EELS line scan and extracted EELS analysis of (f) LGO and (g) Pd NPs corresponding to the multilayer films.

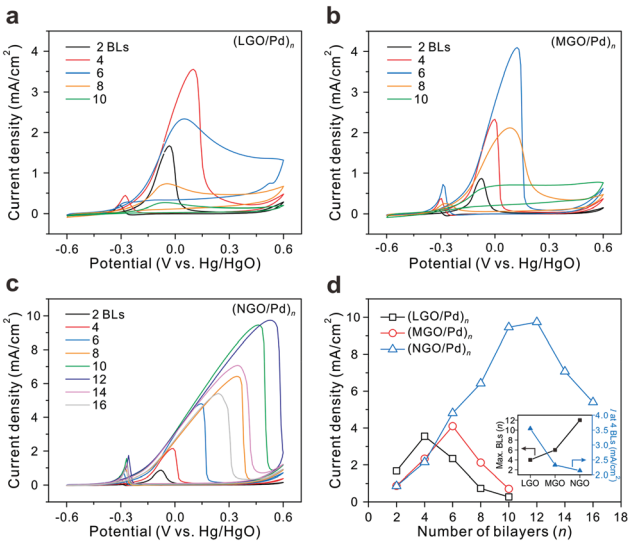

Fig. 5 (a–c) Cyclic voltammograms (CVs) of (a) $(LGO/Pd)_n$, (b) $(MGO/Pd)_n$, and (c) $(NGO/Pd)_n$ multilayer thin film electrodes. (d) Comparison of the electrochemical performance toward the MOR as a function of the number of BLs. The inset in d shows the maximum number of BLs for all multilayer thin films and the current density at 4 BLs. All CVs were recorded in N_2 saturated 0.10 M KOH with 1.0 M CH_3OH at a scan rate of 20 mV s^{-1}.

properties of 3D electrodes with respect to the electrochemical process. Compared to the fast kinetics of a redox probe such as ferricyanide, the methanol oxidation kinetics are sluggish. Additionally, the diffusion of the methanol molecules into the inner electrode significantly influences the overall catalytic performance.[36,37,48,49] In our previous study, the maximum catalytic effect for methanol oxidation was found at a specific number of BLs in graphene-supported metallic multilayers due to the limited diffusion of methanol into the 3D electrode by the layered architecture of 2D GO sheet building blocks, resulting in a conversion from a surface-confined process to a diffusion-limited process as the film thickness was increased.[50] It is of note that this layer-dependence of the electrochemical operating principle is a unique characteristic of LbL-assembled multilayer electrodes.

Interestingly, in this study, the larger-sized GO sheet-supported $(LGO/Pd)_n$ multilayers showed a maximum current density of 3.55 mA cm^{-2} at only 4 BLs (Fig. 5a). This indicates that the methanol diffusion pathways were limited at an early stage by the balance between the mass and charge transfer processes, compared to that of the $(MGO/Pd)_n$ films that saturated at 6 BLs (Fig. 5b). Most interestingly, the $(NGO/Pd)_n$ films, which have many more diffusion pathways, yielded the highest current value of 9.74 mA cm^{-2} at 12 BLs (Fig. 5c). Accordingly, we found that a higher number of BLs were required for the maximum catalytic effect in smaller-sized NGO. This highlights the enhanced mass transfer of the methanol reactants resulting from facile diffusion through the multiple pathways created within the multilayer electrodes integrated with NGO. The chronoamperometric measurement of electrocatalytic performance is in accord with the current density values measured in CVs (see Fig. S6 in the ESI†). It also exhibited the high stability owing to the stable graphene nanosheet supports for electroactive metal NPs.

Fig. 5d summarizes the relationship between mass and charge transfer with varying GO sheet sizes. In terms of charge

 This journal is © The Royal Society of Chemistry 2018

Published on 30 July 2018. Downloaded by Ulsan National Institute of Science & Technology (UNIST) on 8/20/2018 1:57:25 AM.

transfer processes, it is generally reported that GO sheets of a smaller size have a lower conductivity than large-sized GO sheets because of the increased degree of oxidation. As a result, the current density of each multilayer electrode compared at 4 BLs, at which the $(LGO/Pd)_n$ film displayed its maximum current density, decreased with decreasing GO sheet size, indicating a trade-off between the mass and charge transfer properties of the graphene-based multilayer electrodes.

Electrochemical impedance spectroscopy (EIS) was performed to evaluate the electrochemical kinetics and interfacial resistance with respect to the charge transfer processes that are critical in electrochemical reactions (Fig. 6a). The charge-transfer resistance (R_{CT}) values obtained from the Nyquist plot semicircles of the $(LGO/Pd)_4$, $(MGO/Pd)_4$, and $(NGO/Pd)_4$ multilayer films were 122, 1115, and 900 Ω, respectively, at −0.1 V. These results demonstrate that the $(LGO/Pd)_4$ film exhibits a higher current density than the $(MGO/Pd)_4$ and $(NGO/Pd)_4$ films due to facile charge transfer resulting from the higher conductivity of larger-sized GO sheets with a lower defect density. This is in accordance with the defect densities determined from FT-IR measurements and the low I_D/I_G ratio of the LGO sheets determined from Raman spectroscopy measurements. Conversely, with regard to the mass-transfer process, the number of BLs at which the films displayed their maximum current density increased with decreasing GO sheet size. Additionally, the electrode assembled with smaller GO sheets also displayed their highest current density at a larger overpotential compared to other films, which was attributed to the alleviation of reactant depletion by enhancing the methanol mobility into the 3D electrode through increased diffusion pathways within the multilayer. In order to quantitatively determine the effects of enhanced mass transfer, the diffusion coefficient (D) was calculated for the $(LGO/Pd)_n$, $(MGO/Pd)_n$, and $(NGO/Pd)_n$ multilayer electrodes, where n is above 6 because the thin layer films such as 2 and 4 BLs are not governed by the diffusion-limited process, but the surface-confined charge-transfer process as demonstrated similarly in our previous study.[37] For an irreversible diffusion-limited process such as the MOR, the current (i) and peak current (i_p) are given by eqn (3) and (4):

$$i = FAC_O^* D_O^{1/2} \nu^{1/2} \left(\frac{\alpha F}{RT}\right)^{1/2} \pi^{1/2} \chi(bt) \quad (3)$$

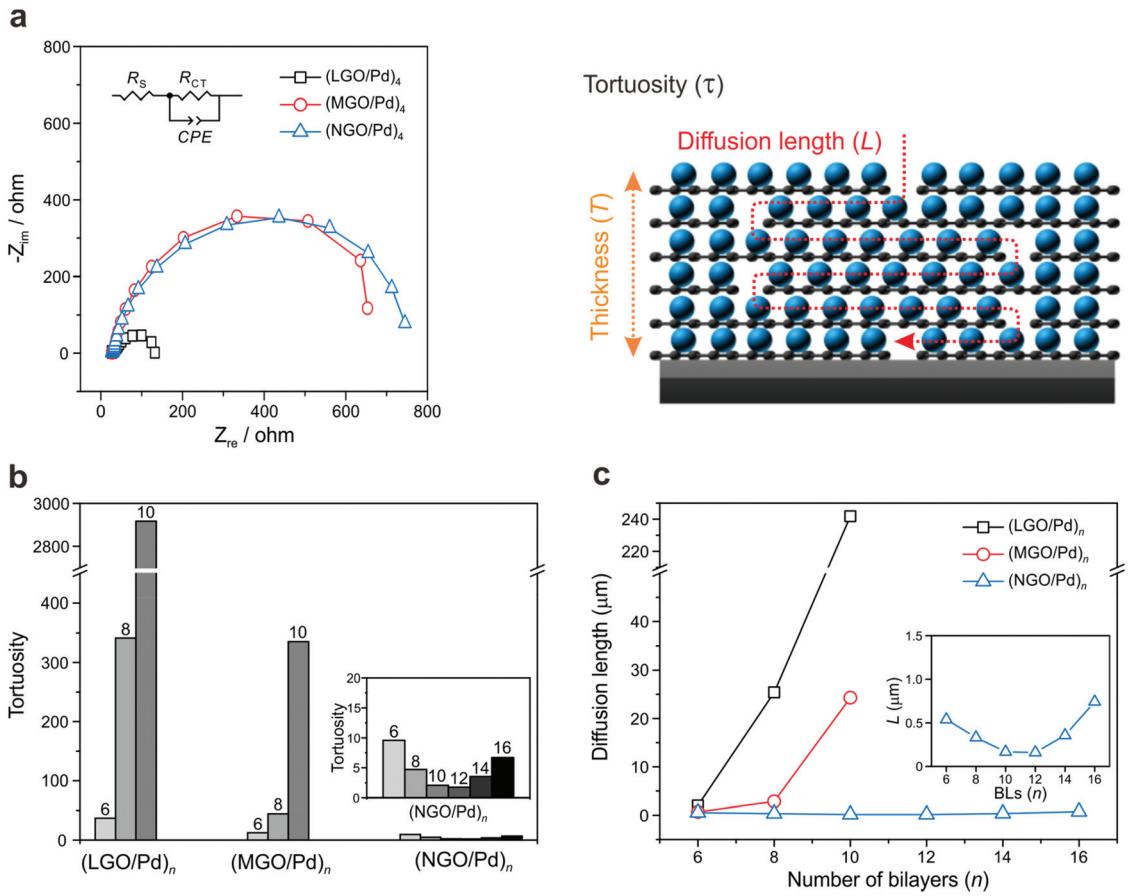

Fig. 6 (a) Nyquist plots of impedance of $(LGO/Pd)_4$, $(MGO/Pd)_4$, and $(NGO/Pd)_4$ multilayer thin films at −0.1 V with an equivalent circuit. (b) The calculated tortuosity and (c) diffusion length of $(LGO/Pd)_n$, $(MGO/Pd)_n$, and $(NGO/Pd)_n$ multilayer thin films with cross-sectional schematic representation of multilayer thin films, where n is above 6. The inset in b and c shows the magnified tortuosity and diffusion length of $(NGO/Pd)_n$ with respect to the bilayer numbers (n), respectively.

Published on 30 July 2018. Downloaded by Ulsan National Institute of Science & Technology (UNIST) on 8/20/2018 1:57:25 AM.

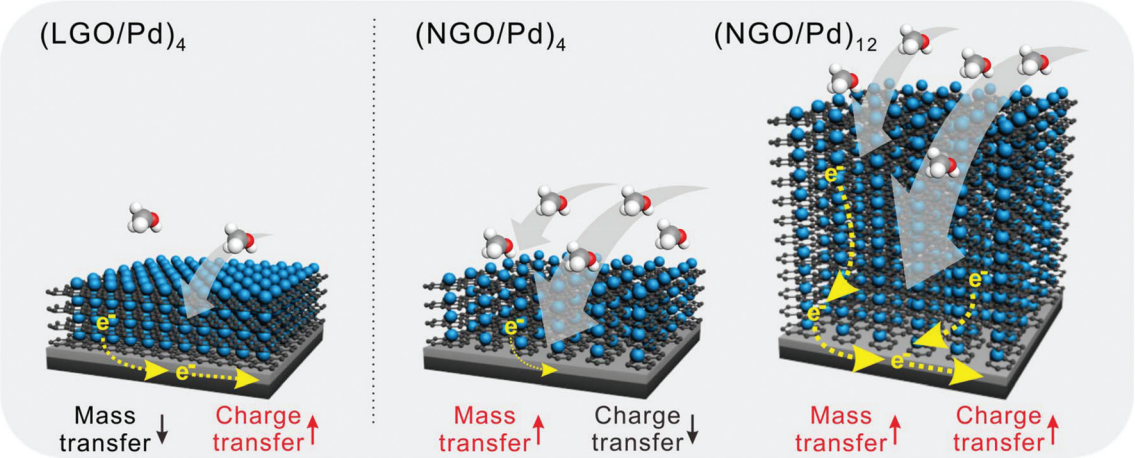

Scheme 2 Schematic representation of the tunable electrocatalytic activity of multilayer electrodes, consisting of Pd NPs assembled with graphene sheets of varying sizes, toward the MOR. The gray and yellow arrows indicate the mass transfer of methanol molecules and the charge transfer, respectively, into the 3D LbL electrodes.

$$i_p = (2.99 \times 10^5)\alpha^{1/2} A C_O^* D^{1/2} \nu^{1/2} \quad (4)$$

where F is the Faraday constant (C mol^{-1}), A is the area (cm^2), C_O^* is the bulk concentration of electroactive components (mol cm^{-3}), ν is the scan rate (V s^{-1}), R is the ideal gas constant (J K^{-1} mol^{-1}), T is the temperature (K), $\chi(bt)$ is a function for the normalized current for an irreversible system, and α is the transfer coefficient. The function $\chi(bt)$ becomes maximum at $\pi^{1/2}\chi(bt) = 0.4958$ for peak current (i_p) and α values were calculated from Tafel slopes, where the number of electrons transferred during the redox reaction, n, was assumed to be 1 because the first charge transfer is the rate determining step in the MOR (see Fig. S7 and Table S1 in the ESI†). $(NGO/Pd)_n$ films show the significantly high D values, which are 160 times higher and 1400 times higher than the D values of $(MGO/Pd)_n$ and $(LGO/Pd)_n$ films, respectively, at 10 BLs. Owing to its superior diffusion properties with a considerably higher D value, the inferior charge-transfer kinetics exhibited by the NGO multilayer electrodes can be overcome by increasing the number of BLs with a high Pd NP mass loading and the overpotential through alleviating reactant depletion at the diffusion-limited region above 0 V, resulting in increased electrocatalytic performance (Scheme 2).

Furthermore, we also calculated two parameters such as tortuosity (τ) and diffusion length (L) of each multilayer film based on eqn (5):

$$\tau = \frac{D}{D_O} = \frac{L}{T} \quad (5)$$

Where D_O is the diffusion coefficient of commercial Pd/C catalysts (see Fig. S8 and Table S1 in the ESI†) and T is the film thickness. As a result, τ of $(NGO/Pd)_n$ films was found to be significantly smaller than other multilayer films in the order of NGO < MGO < LGO as shown in Fig. 6b; for example, as a fixed number of bilayers, the $(NGO/Pd)_{10}$ displayed a τ value of merely 2 in comparison to that of the $(LGO/Pd)_{10}$ film with a considerably higher τ of 2917 (Table S1 in the ESI†). This result suggests that all reactants are directly accessible into the inner catalytic surface of films without taking a detour. In contrast, the $(LGO/Pd)_n$ films should experience a considerably longer and tortuous path which corresponds to longer L with respect to the number of BLs as shown in Fig. 6c. Although developing the electron pathway by increasing the electrical conductivity has been mainly emphasized in the literature when designing efficient electrocatalysts,[51] achieving a facile diffusion pathway is also a critical issue that has not been the subject of intensive study so far. The results presented here reaffirm that establishing the high diffusion pathways, as well as increasing the conductivity, is essential for designing high-performance nanomaterial electrodes.

Conclusions

In conclusion, we developed hybrid electrocatalytic multilayer electrodes for the methanol oxidation reaction composed of Pd NPs supported by GO sheets of varying lateral dimensions. The facile LbL assembled nanoelectrode offers precise control over not only the electrode thickness and composition, but also its catalytic effect by changing the number of BLs. We found that the catalytic activity of multilayered $(GO/Pd)_n$ hybrid electrodes could be tuned by varying the number of BLs and the GO sheet size. The larger-sized GO support showed facile charge transfer in the thinner electrode films, while the smaller-sized graphene support exhibited enhanced mass transfer in the thicker electrode films, indicating a trade-off between the mass and charge transfer within these multilayer electrodes. With this structural control, as well as the versatile nature of the LbL assembly method for building 3D electrodes, we anticipate that this new design will offer a unique opportunity to understand the fundamental electrochemical kinetics of various electrode designs for future energy conversion and storage systems.

 This journal is © The Royal Society of Chemistry 2018

Published on 30 July 2018. Downloaded by Ulsan National Institute of Science & Technology (UNIST) on 8/20/2018 1:57:25 AM.

Conflicts of interest

There are no conflicts to declare.

Acknowledgements

This work was supported by the National Research Foundation of Korea (NRF) grant (2017M3A7B4052802). M. Gu acknowledges financial support from the Global Ph.D. Fellowship funded by the NRF (NRF-2013H1A2A1033278).

References

1 J. A. Turner, *Science*, 1999, **285**, 687–689.
2 M. K. Debe, *Nature*, 2012, **486**, 43–51.
3 N. S. Choi, Z. H. Chen, S. A. Freunberger, X. L. Ji, Y. K. Sun, K. Amine, G. Yushin, L. F. Nazar, J. Cho and P. G. Bruce, *Angew. Chem., Int. Ed.*, 2012, **51**, 9994–10024.
4 D. Larcher and J. M. Tarascon, *Nat. Chem.*, 2015, **7**, 19–29.
5 T. Asefa, *Acc. Chem. Res.*, 2016, **49**, 1873–1883.
6 C. G. Hu and L. M. Dai, *Angew. Chem., Int. Ed.*, 2016, **55**, 11736–11758.
7 E. Lam and J. H. T. Luong, *ACS Catal.*, 2014, **4**, 3393–3410.
8 P. V. Kamat, *J. Phys. Chem. Lett.*, 2010, **1**, 520–527.
9 D. R. Dreyer, S. Park, C. W. Bielawski and R. S. Ruoff, *Chem. Soc. Rev.*, 2010, **39**, 228–240.
10 D. Krishnan, F. Kim, J. Y. Luo, R. Cruz-Silva, L. J. Cote, H. D. Jang and J. X. Huang, *Nano Today*, 2012, **7**, 137–152.
11 T. Lee, S. H. Min, M. Gu, Y. K. Jung, W. Lee, J. U. Lee, D. G. Seong and B. S. Kim, *Chem. Mater.*, 2015, **27**, 3785–3796.
12 H. J. Choi, S. M. Jung, J. M. Seo, D. W. Chang, L. M. Dai and J. B. Baek, *Nano Energy*, 2012, **1**, 534–551.
13 D. W. Chang and J. B. Baek, *Chem. – Asian J.*, 2016, **11**, 1125–1137.
14 I. V. Lightcap and P. V. Kamat, *Acc. Chem. Res.*, 2013, **46**, 2235–2243.
15 A. H. Khan, S. Ghosh, B. Pradhan, A. Dalui, L. K. Shrestha, S. Acharya and K. Ariga, *Bull. Chem. Soc. Jpn.*, 2017, **90**, 627–648.
16 C. L. Tan, X. H. Cao, X. J. Wu, Q. Y. He, J. Yang, X. Zhang, J. Z. Chen, W. Zhao, S. K. Han, G. H. Nam, M. Sindoro and H. Zhang, *Chem. Rev.*, 2017, **117**, 6225–6331.
17 D. Jariwala, T. J. Marks and M. C. Hersam, *Nat. Mater.*, 2017, **16**, 170–181.
18 Q. Q. Li, S. Zhang, L. M. Dai and L. S. Li, *J. Am. Chem. Soc.*, 2012, **134**, 18932–18935.
19 B. Zhang, L. X. Fan, H. W. Zhong, Y. W. Liu and S. L. Chen, *J. Am. Chem. Soc.*, 2013, **135**, 10073–10080.
20 X. L. Wang, H. Bai and G. Q. Shi, *J. Am. Chem. Soc.*, 2011, **133**, 6338–6342.
21 W. J. Zhang, X. F. Zou, H. R. Li, J. J. Hou, J. F. Zhao, J. W. Lan, B. L. Feng and S. T. Liu, *RSC Adv.*, 2015, **5**, 146–152.
22 X. D. Qi, T. N. Zhou, S. Deng, G. Y. Zong, X. L. Yao and Q. Fu, *J. Mater. Sci.*, 2014, **49**, 1785–1793.
23 G. Decher, *Science*, 1997, **277**, 1232–1237.
24 J. J. Richardson, M. Bjornmalm and F. Caruso, *Science*, 2015, **348**, aaa2491.
25 E. Ahn, T. Lee, M. Gu, M. Park, S. H. Min and B.-S. Kim, *Chem. Mater.*, 2017, **29**, 69–79.
26 G. Rydzek, Q. M. Ji, M. Li, P. Schaaf, J. P. Hill, F. Boulmedais and K. Ariga, *Nano Today*, 2015, **10**, 138–167.
27 M. Yang, Y. Hou and N. A. Kotov, *Nano Today*, 2012, **7**, 430–447.
28 M. Gu, J. Lee, Y. Kim, J. S. Kim, B. Y. Jang, K. T. Lee and B. S. Kim, *RSC Adv.*, 2014, **4**, 46940–46946.
29 S. W. Lee, B.-S. Kim, S. Chen, Y. Shao-Horn and P. T. Hammond, *J. Am. Chem. Soc.*, 2009, **131**, 671–679.
30 Y. Choi, S. Choi, H. Y. Jeong, M. Liu, B.-S. Kim and G. Kim, *ACS Appl. Mater. Interfaces*, 2014, **6**, 17352–17357.
31 C. B. Bucur, J. Muldoon and A. Lita, *Energy Environ. Sci.*, 2016, **9**, 992–998.
32 Y. Ko, D. Shin, B. Koo, S. W. Lee, W. S. Yoon and J. Cho, *Nano Energy*, 2015, **12**, 612–625.
33 S. W. Lee, B. M. Gallant, H. R. Byon, P. T. Hammond and Y. Shao-Horn, *Energy Environ. Sci.*, 2011, **4**, 1972–1985.
34 J. W. Jeon, S. R. Kwon and J. L. Lutkenhaus, *J. Mater. Chem. A*, 2015, **3**, 3757–3767.
35 T. Lee, T. Yun, B. Park, B. Sharma, H. K. Song and B. S. Kim, *J. Mater. Chem.*, 2012, **22**, 21092–21099.
36 Y. Choi, M. Gu, J. Park, H. K. Song and B. S. Kim, *Adv. Energy Mater.*, 2012, **2**, 1510–1518.
37 M. Gu and B. S. Kim, *Nano Energy*, 2016, **30**, 658–666.
38 H. Ishihara, Y. C. Chen, N. De Marco, O. Lin, C. M. Huang, V. Limsakoune, Y. C. Chou, Y. Yang and V. Tung, *Sci. Rep.*, 2016, **6**, 38701.
39 Y. C. Chen, A. Y. Lu, P. Lu, X. L. Yang, C. M. Jiang, M. Mariano, B. Kaehr, O. Lin, A. Taylor, I. D. Sharp, L. J. Li, S. S. Chou and V. Tung, *Adv. Mater.*, 2017, **29**, 1703863.
40 W. S. Hummers and R. E. Offeman, *J. Am. Chem. Soc.*, 1958, **80**, 1339–1339.
41 L. Y. Niu, J. N. Coleman, H. Zhang, H. Shin, M. Chhowalla and Z. J. Zheng, *Small*, 2016, **12**, 272–293.
42 M. S. Chang, Y. S. Kim, J. H. Kang, J. Park, S. J. Sung, S. H. So, K. T. Park, S. J. Yang, T. Kim and C. R. Park, *Chem. Mater.*, 2017, **29**, 307–318.
43 J. Luo, L. J. Cote, V. C. Tung, A. T. L. Tan, P. E. Goins, J. Wu and J. Huang, *J. Am. Chem. Soc.*, 2010, **132**, 17667–17669.
44 D. I. Gittins and F. Caruso, *Angew. Chem., Int. Ed.*, 2001, **40**, 3001–3004.
45 M. Park, K. Song, T. Lee, J. Cha, I. Lyo and B.-S. Kim, *ACS Appl. Mater. Interfaces*, 2016, **8**, 21595–21602.
46 M. A. Priolo, K. M. Holder, T. Guin and J. C. Grunlan, *Macromol. Rapid Commun.*, 2015, **36**, 866–879.
47 J. H. Choi, Y. W. Park, T. H. Park, E. H. Song, H. J. Lee, H. Kim, S. J. Shin, V. L. C. Fai and B.-K. Ju, *Langmuir*, 2012, **28**, 6826–6831.

Published on 30 July 2018. Downloaded by Ulsan National Institute of Science & Technology (UNIST) on 8/20/2018 1:57:25 AM.

48 J. Kim, S. W. Lee, P. T. Hammond and Y. Shao-Horn, *Chem. Mater.*, 2009, **21**, 2993–3001.
49 D. Wang, J. Wang, Z.-e. Liu, X. Yang, X. Hu, J. Deng, N. Yang, Q. Wan and Q. Yuan, *ACS Appl. Mater. Interfaces*, 2016, **8**, 28265–28273.
50 K. Jo, M. Gu and B.-S. Kim, *Chem. Mater.*, 2015, **27**, 7982–7989.
51 D. G. Lee, O. Gwon, H. S. Park, S. H. Kim, J. Yang, S. K. Kwak, G. Kim and H. K. Song, *Angew. Chem., Int. Ed.*, 2015, **54**, 15730–15733.

 This journal is © The Royal Society of Chemistry 2018